ISPRS Journal of Photogrammetry and Remote Sensing 142 (2018) 190–204

Contents lists available at ScienceDirect

ISPRS Journal of Photogrammetry and Remote Sensing

journal homepage: www.elsevier.com/locate/isprsjprs

Comprehensive assessment of four-parameter diurnal land surface temperature cycle models under clear-sky

Falu Hong[a], Wenfeng Zhan[a,b,*], Frank-M. Göttsche[c], Zihan Liu[a], Ji Zhou[d], Fan Huang[a], Jiameng Lai[a], Manchun Li[a]

[a] Jiangsu Provincial Key Laboratory of Geographic Information Science and Technology, International Institute for Earth System Science, Nanjing University, Nanjing, Jiangsu 210023, China
[b] Jiangsu Center for Collaborative Innovation in Geographical Information Resource Development and Application, Nanjing 210023, China
[c] Karlsruhe Institute of Technology (KIT), Hermann-von-Helmholtz-Platz 1, 76344 Eggenstein-Leopoldshafen, Germany
[d] School of Resources and Environment, Information Geoscience Research Center, University of Electronic Science and Technology of China, Chengdu, Sichuan 610054, China

ARTICLE INFO

Keywords:
Land surface temperature
Diurnal temperature cycle
Polar-orbiting satellite
Thermal remote sensing
Model comparison

ABSTRACT

Diurnal land surface temperature cycle (DTC) models are useful tools for generating continuous diurnal land surface temperature (LST) dynamics from temporally sparse satellite observations. Four-parameter DTC models (FPD) can be applied to tandem polar-orbiting satellite observations that sample the surface at least four times per day and, therefore, they have received especial attention. Different approaches have been proposed to reduce the parameter number of DTC models to only four, but a comprehensive and systematic comparison of the published FPDs and their performance is lacking. In addition, it remains unclear whether there are even better parameter-reduction approaches (PRAs) for DTC modeling when only four observations per day are available. Consequently, we chose three semi-empirical DTC models (GOT01, INA08, and GOT09) and one quasi-physical DTC model (GEM) and obtained nine FPDs with PRAs (e.g., by fixing some of the DTC parameters as constants). Using *in-situ* thermal observations from the U.S. Climate Reference Network, as well as LSTs from the geostationary MSG and FY-2F satellites under clear sky, we compared the performances of these nine FPDs for 24 and 4 available LST observations per day. We obtained the following results: (1) The GOT09- and GEM-type models generally performed better than the other models with *in-situ* measurements, while the INA08-ts and GOT09-type models possessed high accuracies for the geostationary LSTs. (2) For the semi-empirical models, the PRA '$t_s = t_{ss} - 1$' (where t_s and t_{ss} are the onsets of nighttime cooling and sunset, respectively) is generally more accurate than the PRA '$\delta T = 0$' (where δT is the day-to-day change of residual temperature). The only exception is the GOT09-type model, for which the '$t_s = t_{ss} - 1$' strategy is less accurate. (3) GOT09-dT-τ, which fixes δT as zero and the atmospheric optical thickness (τ) as 0.01 for parameter reduction, shows the best performance of the FPDs. The study gives an overview of commonly-used four-parameter DTC models, provides a foundation for generating spatio-temporally continuous LST products, and offers guidance for choosing four-parameter DTC models in various applications.

1. Introduction

As one of the key parameters of land-atmosphere energy exchange, land surface temperature (LST) has been widely used in various disciplines, including meteorology and climate, hydrology, and ecology (Anderson et al., 2008; Karnieli et al., 2010; Qiao et al., 2013; Wan and Li, 1997; Weng, 2009). Compared with traditional *in-situ* measurements, satellite thermal remote sensing has become increasingly attractive because of its ability to obtain LSTs regularly over an extensive region. However, there is a tradeoff between the spatial and temporal resolutions of most satellite observations, which results in a temporally discontinuous or even sporadic sampling of the surface and hinders the retrieval of continuous LST fields. Fortunately, the temporally continuous LST dynamics can be reconstructed using diurnal temperature cycle (DTC) models. By assisting the generation of temporally continuous LSTs, DTC models (or diurnal LST dynamics) have demonstrated their value for the retrieval of LST and emissivity (Jiang et al., 2006), reconstruction of spatio-temporally continuous and/or

* Corresponding author at: Nanjing University at Xianlin Campus, No. 163, Xianlin Avenue, Qixia District, Nanjing, Jiangsu Province, 210023, China.
E-mail addresses: hongfalu@foxmail.com (F. Hong), zhanwenfeng@nju.edu.cn (W. Zhan), frank.goettsche@kit.edu (F.-M. Göttsche), rs312lzh@yeah.net (Z. Liu), jzhou233@uestc.edu.cn (J. Zhou), nju_huangfan@163.com (F. Huang), NJULJM@126.com (J. Lai), manchun@nju.edu.cn (M. Li).

https://doi.org/10.1016/j.isprsjprs.2018.06.008
Received 10 January 2018; Received in revised form 29 April 2018; Accepted 10 June 2018
Available online 15 June 2018

consistent LSTs (Duan et al., 2014a; Göttsche and Olesen, 2001; Holmes et al., 2016; Inamdar et al., 2008; Liu et al., 2017), estimation of LST under cloudy condition (Zhang et al., 2015), downscaling/disaggregation of LSTs (Quan et al., 2014; Zhan et al., 2016), estimation of surface air temperatures (Bechtel et al., 2014, 2017; Gholamnia et al., 2017; Zakšek and Schroedter-Homscheidt, 2009), derivation of surface thermal properties (Holmes et al., 2015; Sobrino and El Kharraz, 1999), temporal extrapolation of surface fluxes (Hain and Anderson, 2017), and the monitoring of diurnal surface urban heat islands (Weng and Fu, 2014; Zakšek and Oštir, 2012; Zhou et al., 2013).

Among the DTC models, the quasi-physical model (QPM) and semi-empirical model (SEM) are the two prevalent categories (Huang et al., 2014). Using heat flux as the key variable, the QPM acquires the LST dynamics formula by parameterizing the surface flux components within the surface energy balance equation (Cracknell and Xue, 1996; Huang et al., 2014; Price, 1977; Sobrino and El Kharraz, 1999; Xue and Cracknell, 1995; Zhan et al., 2014). The QPM is relatively complex and its parameter number may range from two to twelve. By comparison, the SEM describes LST dynamics directly using LST as the key variable, and models its dynamics by empirical functions (Göttsche and Olesen, 2001, 2009; Inamdar et al., 2008; Parton and Logan, 1981; Sun and Pinker, 2005; Van Den Bergh et al., 2007). The structure of the SEM is generally relatively simple and its parameter number typically ranges from three to six.

There is a tradeoff between modeling accuracy and the parameter number of DTC models. DTC models with more parameters usually possess higher accuracies (Duan et al., 2012; Huang et al., 2014), but are usually less applicable to satellite LST with a relatively low temporal resolution, e.g., when there are fewer daily overpasses than free model controlling parameters (Duan et al., 2014b). In contrast, DTC models with fewer parameters usually reproduce the input data with lower accuracy, but they are better suited to modelling satellite data with fewer daily overpasses (Huang et al., 2014; Watson, 2000).

DTC models were initially applied to hourly or sub-hourly thermal data from geostationary satellites with relatively coarse spatial resolutions (around 3–5 km). Such a coarse resolution, however, greatly limits the applications that require fine-scale thermal data for the surfaces (Duan et al., 2014b; Inamdar et al., 2008). LST products obtained by tandem polar-orbiting satellite systems (e.g., AVHRR and MODIS) can provide four overpasses per day, have a finer spatial resolution (around 1 km), complement the coarse geostationary LSTs, and have been widely used in related applications (Imhoff et al., 2010; Vancutsem et al., 2010; Wan et al., 2004). But with only the four transits within a diurnal cycle, important features on the diurnal variations of specific applications (e.g., for monitoring of urban heat islands) may be missed (Duan et al., 2014a; Zakšek and Oštir, 2012). Consequently, four-parameter DTC models (hereafter termed FPDs) have received especial attention, since they can fully reconstruct diurnal LST dynamics with only four observations (Duan et al., 2014b). The FPDs have demonstrated their utility for many applications requiring full DTC information: e.g., the timing of daily maximum LST, estimation of diurnal mean LST and diurnal LST range, and retrieval of surface thermal inertia (Holmes et al., 2013; Sobrino and El Kharraz, 1999; Zhan et al., 2014).

Due to their usefulness, great progress has been achieved in developing FPDs. Generally, FPDs can be divided into two categories: The first focuses on reducing the parameter number of the DTC models to four, by fixing one or more of their parameters as constants for individual cases. For example, Schädlich et al. (2001) assumed that the day-to-day change of residual temperature (i.e., δT) of semi-empirical DTC models approximates to zero in simple cases; Holmes et al. (2013) suggested that the start of the attenuation function (termed t_s) can be equated to the time when the temperature has decreased to half its maximum value; and Duan et al. (2014b) proposed that t_s is often exactly one hour before sunset (t_{ss}). Similarly, by the parameterization of the upward surface fluxes, FPDs can be directly derived from quasi-physical model DTC models (Huang et al., 2014; Sobrino and El Kharraz, 1999; Zhan et al., 2014). For the second FPD category, DTC models with more than four parameters are solvable using only four daily observations when additional information (e.g., from the temporally or spatially adjacent LST pixels) is incorporated. The additional information/knowledge can be the monthly LST dynamics obtained from land surface models, or geostationary LSTs that provide a background field for solving DTC models (Aires et al., 2004; Jin and Dickinson, 1999; Sun and Pinker, 2005; Zhou et al., 2013); day-to-day temperature continuity within a multi-day period (Duan et al., 2013); or the consistency of component temperature dynamics within neighboring pixels (Quan et al., 2014).

In addition to the temporal continuum or spatial consistency hypothesis, the second category of FPDs is relatively complex and may induce additional uncertainties caused by the ancillary data used for derivation of component information. By contrast, the structure of the first category of FPDs is relatively simple, and they can be operated based on LST data within a single day for a single pixel. In other words, the first category of models has the advantage to be implemented more easily and can therefore be more suitable for related applications. Previous parameter-reduction approaches (PRAs) were only tested on a single specific DTC model. The reduced parameters as shown (e.g., δT and t_s) appear in most of the five-parameter semi-empirical DTC models including GOT01 (Göttsche and Olesen, 2001) and INA08 (Inamdar et al., 2008), as well as the six-parameter semi-empirical DTC model GOT09 (Göttsche and Olesen, 2009). Therefore, these two PRAs can be applied to all these models. In addition, the parameter number of the QPM can be adjusted to four if specific parameterization schemes are used (Huang et al., 2014; Zhan et al., 2014).

With suitable PRAs, it is expected that several FPDs can be generated; however, several challenges remain for these potential models: First, a comprehensive assessment of the performances of these potential FPDs is lacking; and second, it remains unclear whether there exist PRAs that are able to generate FPDs with even higher accuracies. To address these issues, the present study aimed to compare both the hourly and overall performances of the FPDs, and further to identify the best FPDs under different cases. Our study is based on several *in-situ* thermal measurements within very different biomes, as well as LSTs retrieved from geostationary satellites across an extensive scale. Our findings are potentially useful for selecting FPDs for practical applications, and for the generation of temporally continuous LST data from four overpasses in a daily cycle; thus, they are also potentially useful for related applications.

2. Data

To cover as many land cover types across the globe and to use as many data sources under various bioclimates as possible, we incorporated both *in-situ* surface temperatures and LSTs obtained from geostationary satellites (Fig. 1). The *in-situ* LSTs were collected by the United States Climate Reference Network (USCRN) (Fig. 1a), while the LSTs were retrieved by the Land Surface Analysis Satellite Application Facility (LSA SAF) from the Spinning Enhanced Visible and Infrared Imager (SEVIRI) onboard Meteosat Second Generation (MSG), operated by the European Organisation for the Exploitation of Meteorological Satellites (Fig. 1b), as well as by the FengYun-2F (FY-2F), operated by the Chinese Meteorological Administration National Satellite Meteorological Center (Fig. 1c).

2.1. In-situ measurements

We chose the *in-situ* measurements from the USCRN because this network contains surface cover types with a sufficient number of varieties spanning very different bioclimates. The USCRN provides observations of most of the basic meteorological variables at 5-minute intervals, including air temperature, LST, wind speed, and relative humidity. The 5-minute LST data (i.e., 288 observations in a single day)

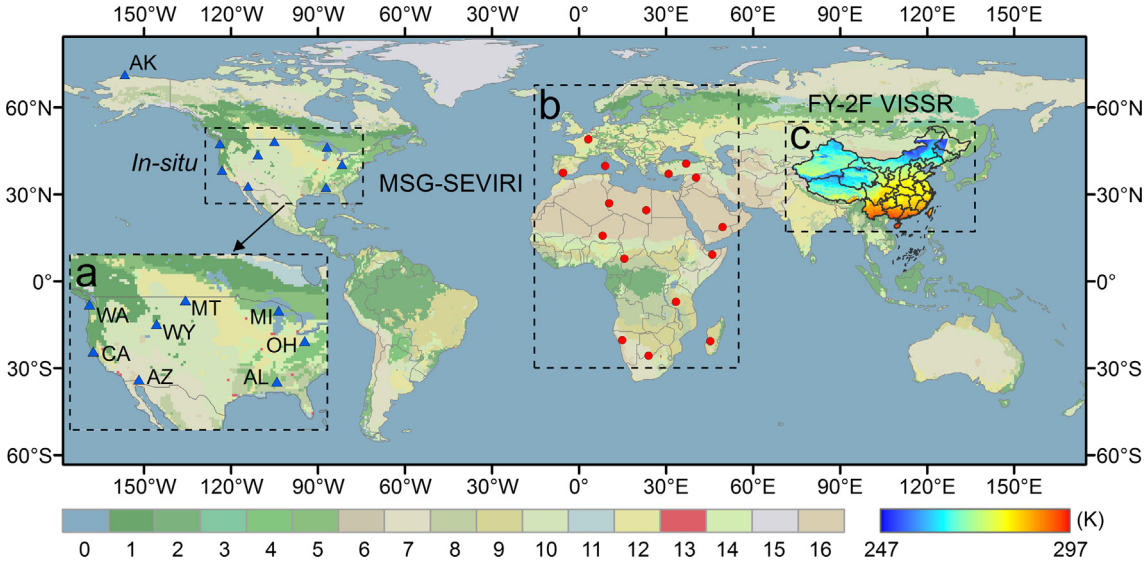

Fig. 1. Geolocations of the sites (regions) where the associated diurnal LSTs cycles were obtained. (a) region where *in-situ* measurements were used, blue triangles representing site locations; (b) region where MSG-SEVIRI LSTs were obtained, red solid circles representing the chosen pixel locations; and (c) region where FY-2F LSTs were used; the color representing the LST value after temporal aggregation. The numbers '0' to '16' denote the corresponding land cover types under the International Geosphere–Biosphere Programme (Friedl et al., 2002). (For interpretation of the references to color in this figure legend, the reader is referred to the web version of this article.)

Table 1
The selected USCRN sites and the number of clear-sky diurnal cycles of *in-situ* data.

Climate zone	Site name	Long./Lat.	Elevation (m)	Day number	Land cover type
Tundra	AK Barrow 4	156.61W/71.32N	5	7	Grass
Humid Subtropical	AL Selma 13	87.24W/32.46N	62	12	Grass
Mid-latitude Desert	AZ Yuma 27	114.19W/32.84N	189	23	Bare soil
Mediterranean	CA Bodega 6	123.07W/38.32N	12	7	Shrub
Humid Continental (cool summer)	MI Chatham 1	86.92W/46.33N	277	9	Grass
Semiarid Steppe	MT Wolf Point 29	105.1W/48.31N	623	9	Grass
Humid Continental (warm summer)	OH Coshocton 8	81.78W/40.37N	313	8	Tree
Marine Westcoast	WA Quinault 4	123.81W/47.51N	97	9	Grass
Highland Alpine	WY Moose 1	110.71W/43.66N	1972	18	Grass

were used to evaluate the performances of the FPDs. It should be noted that brightness temperature (BT), rather than LST, was provided by the USCRN (i.e., the emissivity effect was not considered); however, previous studies have indicated that comparison of model performances is still possible because the use of BTs has only a limited effect on model performance (Göttsche and Olesen, 2001; Huang et al., 2014; Van Den Bergh et al., 2007). We chose sites with relatively homogeneous terrains and continuous land cover types; i.e., the measurements of diurnal surface temperatures are minimally impacted by adjacent surface objects such as high trees and/or mountains, because these undulations would likely alter the LST dynamics because of the induced shadows, especially when the solar altitude is low. To include the diurnal LST dynamics of a sufficient number of land cover types within different bioclimates, we finally selected nine sites, each representing a typical land surface type within a specific bioclimate, over which a total of 102 diurnal cycles ranging from 2013 to 2015 were used for comparison (Table 1). For each site, at least seven diurnal cycles over different seasons were identified to represent possible land cover change due to vegetation phenology.

2.2. LSTs obtained from geostationary satellites

(1) MSG-SEVIRI data

SEVIRI samples the surface every 15 min; i.e., 96 observations can be obtained in a single diurnal cycle. In addition, its LST product has a 3-km sampling distance at nadir. The LSTs were retrieved by LSA SAF (Trigo et al., 2011) with a split-window algorithm; it has an accuracy of around 1.0 K (Freitas et al., 2010; Göttsche et al., 2016). We chose 111 diurnal cycles of SEVIRI LSTs under clear sky in 2016. These cycles were obtained over pixels covered by multiple land cover types in different seasons (see Fig. 1b and Table 2). The quality control flags of the SEVIRI LSTs are either equal to or above the nominal, which

Table 2
Elaborate information on the selected MSG-SEVIRI pixels under clear sky.

Site	Long./Lat.	Day num.	Elevation (m)	Land cover type
1	5.53W/37.46N	4	77	Croplands
2	3.18E/49.03N	2	141	Croplands
3	30.95E/37.12N	7	157	Closed shrublands
4	40.36E/35.81N	11	320	Barren or sparsely vegetated
5	49.55E/18.75N	8	349	Open shrublands
6	9.02E/39.78N	6	369	Closed shrublands
7	23.24E/24.52N	18	388	Barren or sparsely vegetated
8	45.30E/20.74S	7	397	Savannas
9	8.10E/15.72N	5	509	Open shrublands
10	15.64E/7.86N	5	512	Wood Savannas
11	10.40E/26.92N	14	558	Barren or sparsely vegetated
12	36.97E/40.58N	5	571	Croplands
13	46.02E/9.22N	4	798	Open shrublands
14	14.93E/20.35S	6	1021	Open shrublands
15	24.02E/25.77S	4	1086	Grasslands
16	33.49E/7.10S	5	1279	Croplands

correspond to LST uncertainties between 1.0 and 2.0 K or less than 1.0 K, respectively.

(2) FY-2F VISSR data

The LST products from the Visible Infrared Spin Scan Radiometer (VISSR) onboard the FY-2F, a geostationary satellite launched by China in Jan. 2012, were also used. These VISSR LSTs were also retrieved using a split-window algorithm, with spatial and temporal resolutions of 5 km and 1 h, respectively (Tang et al., 2008). The study employed all the valid (cloud-free) LSTs during Jan. 2016, which cover a large part of Mainland China; northeast China was not included (Fig. 1c). Note that the FY-2F LST data have not been validated extensively and there is no quality control flag available for these data. Therefore, the cloud-free LSTs during this month were temporally aggregated (i.e., temporal compositing) according to their respective acquisition hour across a diurnal cycle to reduce the random errors for the retrieved LSTs. This procedure also aims at obtaining a dataset with as few gaps due to clouds as possible, based on which the pixel-by-pixel assessments of FPDs are feasible. This means that, in contrast to the MSG-SEVIRI data, there is only one DTC model fit per pixel for the FY-2F data.

3. Methodology

3.1. Summary of investigated FPDs

Three types of semi-empirical DTC models, including GOT01 proposed by Göttsche and Olesen (2001), INA08 by Inamdar et al. (2008), and GOT09 by Göttsche and Olesen (2009), and one type of quasi-physical model developed by Huang et al. (2014) and Zhan et al. (2014), were modified using PRAs or adaptions to restrict the number of free parameters to four.

3.1.1. GOT01-type and INA08-type models

GOT01 and INA08, proposed by Göttsche and Olesen (2001) and Inamdar et al. (2008), respectively, are two semi-empirical models with similar formulations. They both use a cosine function to depict LST dynamics during the day, while different empirical functions are used for the nighttime cooling process, with the former/latter employing exponential/hyperbolic functions. The general form of these two models is as follows:

$$\begin{cases} T_{\mathrm{day}}(t) = T_0 + T_a \cos[\pi\omega^{-1}(t-t_{\mathrm{m}})],\ t < t_s \\ T_{\mathrm{nig}}(t) = (T_0 + \delta T) + [T_a \cos[\pi\omega^{-1}(t-t_{\mathrm{m}}) - \delta T]\cdot f(t),\ \ t \geqslant t_s \end{cases} \quad (1)$$

where $T_{\mathrm{day}}(t)$ and $T_{\mathrm{nig}}(t)$ denote the temperature dynamics during the day and night at time t, respectively; T_0 is the residual temperature around sunrise; T_{a} is the temperature amplitude; t_{m} is the time when temperature reaches its maximum; t_{s} is the time when free attenuation begins; δT is the day-to-day change of residual temperature; ω is the half-width of the cosine term and can be determined from the daytime duration; and k is the attention rate of nighttime temperature decrease. The formulas for calculating ω and k are given in Göttsche and Olesen (2001). With $f(t) = \exp[-(t - t_{\mathrm{s}})\cdot k^{-1}]$, Eq. (1) denotes GOT01; while it becomes INA08 with $f(t) = k\cdot(k + t - t_{\mathrm{s}})^{-1}$.

GOT01 and INA08 both contain five parameters (i.e., T_0, T_{a}, t_{m}, t_{s}, and δT). As introduced in Section 1, the parameter number of these two models can be reduced to four by either setting δT to zero (i.e., $\delta T = 0$) (Schädlich et al., 2001) or fixing t_{s} to one hour before sunset (i.e., $t_{\mathrm{s}} = t_{\mathrm{ss}} - 1$, where t_{ss} is the sunset time) (Duan et al., 2014b). Using these two strategies, we obtain four FPDs, including GOT01-dT (i.e., GOT01 with '$\delta T = 0$'), GOT01-ts (i.e., GOT01 with '$t_{\mathrm{s}} = t_{\mathrm{ss}} - 1$'), INA08-dT (i.e., INA08 with '$\delta T = 0$'), and INA08-ts (i.e., INA08 with '$t_{\mathrm{s}} = t_{\mathrm{ss}} - 1$'). Note that t_{s} can also be approximated as the time when half the temperature decrease from maximum has occurred (i.e., $t_{\mathrm{s}} = t_{\mathrm{m}} + \omega\cdot\pi^{-1}\cdot\arccos[0.5(1 + \delta T/T_{\mathrm{a}})]$), as demonstrated by Holmes et al. (2013). The results related to this PRA are given in Appendix A because the PRA under '$t_{\mathrm{s}} = t_{\mathrm{ss}} - 1$' is comparatively simpler and has a better performance.

3.1.2. GOT09-type models

Based on GOT01, Göttsche and Olesen (2009) further considered the relatively slow LST increase after sunrise to be due to the significantly higher total atmospheric optical thickness (TOT) at large sun zenith angles. This revised DTC model is hereafter termed GOT09 and is formulated as follows:

$$\begin{cases} T_{\mathrm{day}}(t) = T_0 + T_a\cos(\theta_{\mathrm{z}})\cos^{-1}(\theta_{\mathrm{z,min}})\cdot e^{[m_{\min} - m(\theta_{\mathrm{z}})]\tau},\ t < t_s \\ T_{\mathrm{nig}}(t) = T_0 + \delta T + \left[T_{\mathrm{a}}\cos(\theta_{\mathrm{zs}})\cos^{-1}(\theta_{\mathrm{z,min}})\cdot e^{[m_{\min} - m(\theta_{\mathrm{zs}})]\tau}\right. \\ \qquad\qquad \left. -\delta T\right] e^{\frac{-12}{\pi k}(\theta - \theta_{\mathrm{s}})},\ \ t \geqslant t_s \end{cases} \quad (2)$$

where θ is the thermal hour angle with respect to thermal noon at time t_{m}, and is calculated as $12^{-1}\cdot\pi\cdot(t - t_{\mathrm{m}})$; θ_{z} is the thermal zenith angle corresponding to θ; $\theta_{\mathrm{z,min}}$ is the minimum zenith angle when $t = t_{\mathrm{m}}$; θ_{s} is the thermal hour angle when $t = t_{\mathrm{s}}$; θ_{zs} is the thermal zenith angle when $\theta = \theta_{\mathrm{s}}$; $m(\theta_{\mathrm{z}})$, $m_{\min}$, and $m(\theta_{\mathrm{zs}})$ are the relative air mass at θ_{z}, $\theta_{\mathrm{z,min}}$, and θ_{zs}, respectively; and τ is the TOT. In total, GOT09 includes six controlling parameters (i.e., T_0, T_{a}, t_{m}, t_{s}, δT, and τ).

The parameter number of GOT09 can be reduced to five by either of the two PRAs (i.e., '$\delta T = 0$' and '$t_{\mathrm{s}} = t_{\mathrm{ss}} - 1$') summarized in Section 3.1.1. For the TOT (i.e., τ), the discussion in Section 5.1 suggests that this variable can be fixed to 0.01 for general use, which yields a new PRA '$\tau = 0.01$' to reduce the number of parameters. Therefore, we obtain three GOT09-type sub-models, termed GOT09-dT-τ, GOT09-ts-τ, and GOT09-dT-ts, wherein 'dT', 'ts', and 'τ' denote the use of the PRA '$\delta T = 0$', '$t_{\mathrm{s}} = t_{\mathrm{ss}} - 1$', and '$\tau = 0.01$', respectively.

3.1.3. GEM-type models

Directly derived from the solution of the heat conduction equation constrained by the surface energy balance equation, Zhan et al. (2014) developed a quasi-physical model (hereafter termed GEM-σ) that only contains four free parameters. GEM-σ can be written as follows:

$$T(t) = T_{\mathrm{d}} + \sigma(t - 0.5\cdot t_{\mathrm{p}}) + \sum_{n=1}^{\infty} M_n\cdot g(t) \quad (3)$$

where T_{d} is the daily average temperature; σ is the rate of change of the day-to-day temperature difference (DTD); t_{p} is the total number of seconds within a daily cycle (i.e., 86,400 s); and M_n and $g(t)$ are two intermediate functions that can be expressed by thermal inertia (P) and the linear coefficient for the upward surface fluxes (h_1) (see Appendix B for more details). Only four controlling parameters, T_{d}, P, h_1, and σ, are needed for GEM-σ.

To better quantify the upward surface fluxes, Huang et al. (2014) disregarded the term related to σ, and further proposed that the linear coefficient of the upward fluxes (i.e., h_1) should not be constant but rather a function of time(t) (i.e., $h_1 = \eta_0 + \eta_1 t$, where η_0 and η_1 are the offset and gain, respectively). This new quasi-physical DTC model also includes four parameters (T_{d}, P, η_1, and η_0) and is hereafter termed GEM-η.

3.1.4. Summary of the FPDs

Through the aforementioned PRAs to the semi-empirical DTC models, and/or the adaptions of the quasi-physical DTC models, we finally acquire nine FPDs for comparison, which are summarized in Table 3.

3.2. Solution of forward FPDs

We employed the Levenberg-Marquardt algorithm to fit the FPDs to the available data and to determine the values of their free parameters. The initial values of the four parameters for each FPD were

Table 3
General information on the nine FPDs used for comparison.

#	Name	Category	Parameters*	PRA
1	GOT01-dT	SEM*	T_0, T_a, t_m, t_s, δT	$\delta T = 0$
2	GOT01-ts	SEM	T_0, T_a, t_m, t_s, δT	$t_s = t_{ss} - 1$
3	INA08-dT	SEM	T_0, T_a, t_m, t_s, δT	$\delta T = 0$
4	INA08-ts	SEM	T_0, T_a, t_m, t_s, δT	$t_s = t_{ss} - 1$
5	GOT09-dT-τ	SEM	T_0, T_a, t_m, t_s, δT, τ	$\delta T = 0$; $\tau = 0.01$
6	GOT09-ts-τ	SEM	T_0, T_a, t_m, t_s, δT, τ	$t_s = t_{ss} - 1$; $\tau = 0.01$
7	GOT09-dT-ts	SEM	T_0, T_a, t_m, t_s, δT, τ	$\delta T = 0$; $t_s = t_{ss} - 1$
8	GEM-σ	QPM	P, T_d h_1, σ	Unnecessary
9	GEM-η	QPM	P, T_d, η_0, η_1	Unnecessary

* SEM and QPM denote semi-empirical and quasi-physical DTC models, respectively.

predetermined according to the local land cover types and background climate (Table 4). Note that the initial values for Site AK Barrow 4 are quite different from the other values because this site is located within the Arctic Circle where extreme conditions (e.g., polar night with extremely low LSTs) occur. The same initial values are used for the δT models (i.e., GOT01-dT, INA08-dT, GOT09-dT-τ and GOT09-dT-ts), the t_s models (i.e., GOT01-ts, INA08-ts, GOT09-ts-τ and GOT09-dT-ts), and the GEM models (Table 4).

3.3. Design of the FPD model comparison

The performance of a DTC model depends on the number and quality of observations used as input. We employed two schemes to fully assess the performances of the FPDs. The first uses hourly data within a daily cycle; i.e., 24 LST observations starting from the hour around sunrise to the same hour of the following day. The second uses only four observations, which are exactly sufficient to resolve the four parameters of the FPDs and which were provided at the times similar to the MODIS overpasses; i.e., 10:30, 13:30, 22:30, and 01:30 (local solar time). The fitting errors of the FPDs are anticipated to be higher under the 4-input than the 24-input schemes, but the relative performance between the FPDs will likely change under the different schemes. We should clarify that the fitting of DTC models in this study was conducted day-by-day owing to the simplicity and robustness of this approach. For the performance assessment of each FPD, we provide both the daily averaged and hourly root mean square errors (RMSEs) between the predicted and original hourly LST data. We use boxplots to illustrate the daily mean error distribution of a certain FPD for DTC modeling over different stations (pixels) and for different diurnal cycles, i.e., the boxplots in Figs. 2, 4, 6, and 8 describe the overall performances of entire day RMSE among all diurnal cycles and stations (pixels). By comparison, only hourly mean errors (without error distributions) of the FPDs are presented in Figs. 3, 5, 7, and 9 to avoid redundancy. With both the *in-situ* and geostationary LSTs and these two different comparison schemes, the model performances are critically compared under four cases, including the *in-situ* data under the 24-input (Case #1) and 4-input schemes (Case #2), and the geostationary data under the 24-input (Case #3) and 4-input schemes (Case #4).

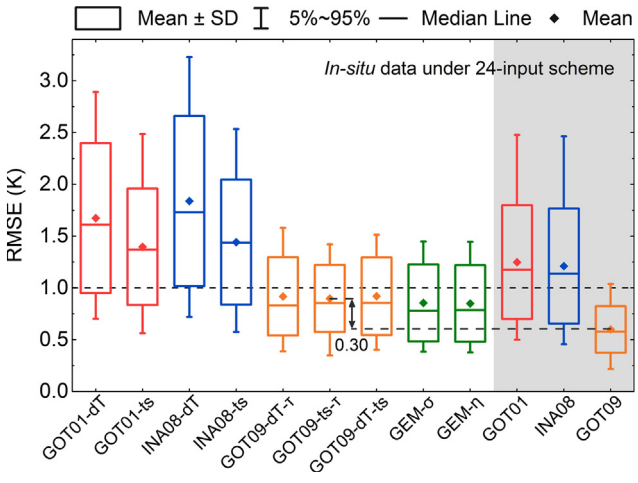

Fig. 2. Boxplots of the overall RMSEs for the nine FPDs under the 24-input scheme with *in-situ* data. The top and bottom whiskers are the 5th and 95th percentile of the RMSEs, respectively; the top and bottom of the box are the mean RMSE plus and minus one standard deviation of the RMSEs, respectively; and the band and point inside the box denote the median and mean RMSE for each model, respectively. The performances of GOT01, INA08, and GOT09 are added as references in the gray shaded area (on the right). The bidirectional arrow shows the accuracy loss caused by using the PRAs '$\delta T = 0$' and '$\tau = 0.01$'; i.e., between GOT09 and the best GOT09-type models (GOT09-ts-τ) with four free parameters.

4. Results

4.1. Case #1: In-situ data under the 24-input scheme

Performance comparisons for the nine FPDs under the 24-input scheme with *in-situ* data during an entire day are shown in Fig. 2 with boxplots. Boxplots of RMSE not only illustrate the mean RMSE of each FPD, they also include the information on the error spread/distribution. To illustrate the model performances over the diurnal cycle, the hourly errors are presented in Fig. 3. In addition, the overall and hourly RMSEs of the original models (including GOT01, INA08, and GOT09) that possess more than four free parameters are also added as references in Figs. 2 and 3 to evaluate the accuracy loss caused by using the specific PRAs.

Under this case, the results show that the original models with more than four free parameters, including GOT01, INA08, and GOT09, all

Table 4
Initial values of the controlling parameters for the nine FPDs used for comparison.

Parameter (unit)	δT series	t_s series	GOT09-dT-ts	GEM-η	GEM-σ
T_0 (K)	T_{min}*	T_{min}	T_{min}	–	–
T_a (K)	T_{max}* − T_{min}	T_{max} − T_{min}	T_{max} − T_{min}	–	–
t_m (h)	13	13	13	–	–
t_s (h)	$t_s = t_{ss} - 1$	–	–	–	–
δT (K)	–	0	–	–	–
τ	–	–	0.01	–	–
P (J m^{-2} K^{-1} s$^{-1/2}$)	–	–	–	700	700
T_d (K)	–	–	–	T_{mean}*	T_{mean}
η_0 (W m^{-2} K^{-1})	–	–	–	10	–
η_1 (W m^{-2} K^{-1} s^{-1})	–	–	–	0	–
h_1 (W m^{-2} K^{-1})	–	–	–	–	10
σ (K s^{-1})	–	–	–	–	0

* T_{min}, T_{max}, and T_{mean} represent the daily minimum, maximum, and mean input LST observations, respectively.

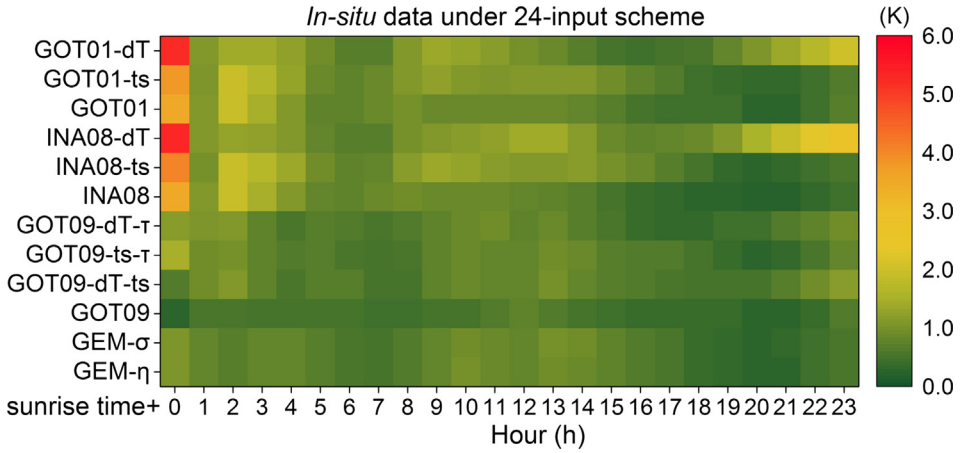

Fig. 3. Hourly RMSEs at each local solar time since sunrise for the nine FPDs, under the 24-input scheme with *in-situ* data. The performances of GOT01, INA08, and GOT09 are added as references.

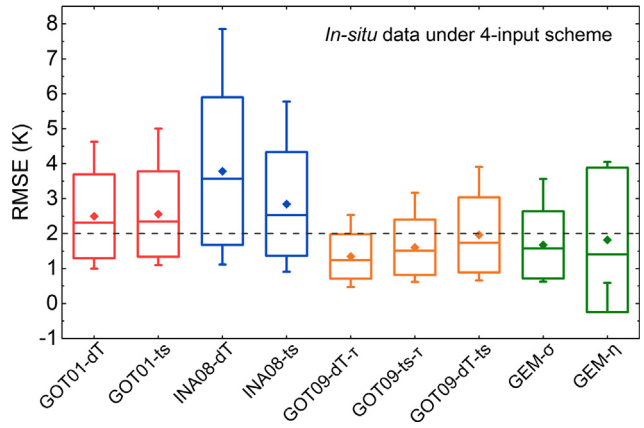

Fig. 4. Same as Fig. 2, but without the reference under the 4-input scheme.

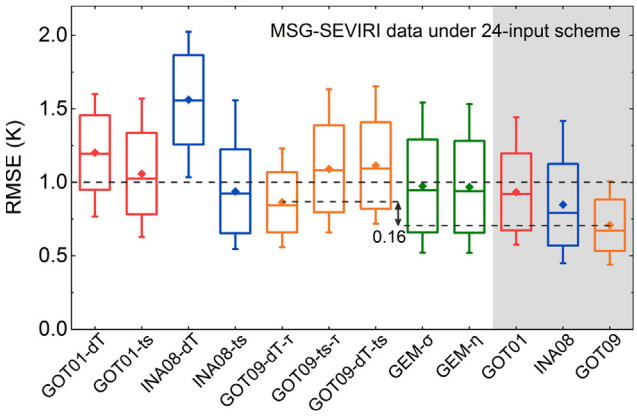

Fig. 6. Same as Fig. 2, but for the MSG-SEVIRI LSTs.

perform better than the corresponding FPDs that are of the same type. Nevertheless, the loss of accuracy caused by using PRAs remains small – only 0.15 K for the GOT01-type models, 0.23 K for the INA08-type models, and 0.30 K for the GOT09-type models (GOT09-ts-τ). The relative reduction in accuracy for the GOT09-type models can be attributed to the loss of two free parameters (i.e., from six to only four).

Among all the FPDs, the GOT09- and GEM-type models perform significantly better than the GOT01- and INA08-type models. Moreover, they perform even better than GOT01 and INA08 with five free parameters (Fig. 2): the mean RMSEs of the GOT09- and GEM-type models are close to or slightly lower than 1.0 K, while the mean RMSEs of the GOT01- and INA08-type models are around 1.5 K. The hourly comparisons reveal that the overall better performances of the GOT09- and GEM-type models are mostly attributable to their superior capability of modelling the relatively slow LST increase after sunrise (see Fig. 3), which is due to the much longer atmospheric path and the weaker solar radiation reaching the surface at that time. Specifically, the GOT09-type models accommodate this slow LST increase by adding TOT (τ) as a controlling variable (Göttsche and Olesen, 2009). The GEM-type models have considered this sluggish LST increase since at least Watson

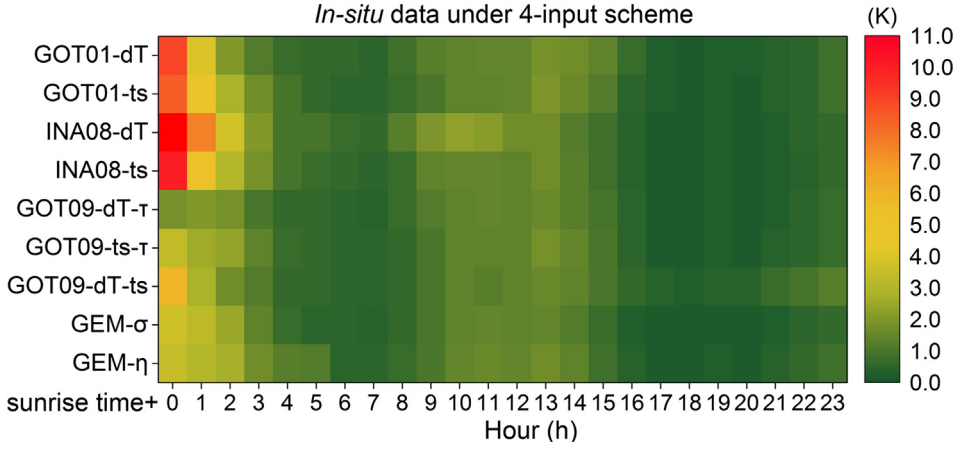

Fig. 5. Same as Fig. 3, but without the reference under the 4-input scheme.

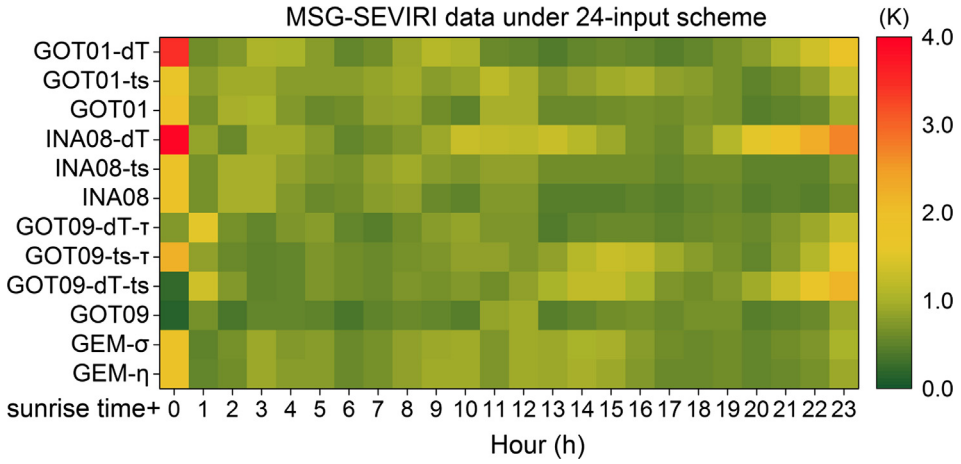

Fig. 7. Same as Fig. 3, but for the MSG-SEVIRI LSTs.

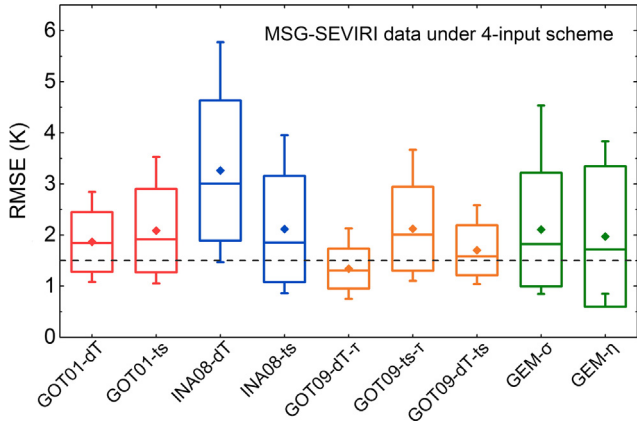

Fig. 8. Same as Fig. 6, but for the 4-input scheme.

(1975), in which an attenuation function of the solar radiation similar to that used by Göttsche and Olesen (2009) was adapted.

The results shown in Fig. 3 reveal that this specific consideration maintains mean prediction RMSEs of the GOT09- and GEM-type models at approximately 1.0 K around sunrise, while for the other models RMSEs increase to 3.0 K or higher. Our results also reveal that the prediction RMSEs of the three GOT09-type models are quite similar (Fig. 3). Interestingly, this finding suggests that the high performance around sunrise is retained even when TOT (τ) is set as a constant (i.e., 0.01), as indicated by the roughly equal performance between the three GOT09-type models.

Among the five models with higher accuracies, the two GEM-type models (i.e., GEM-σ and GEM-η) perform marginally better than the three GOT09-type models (Fig. 2). This is probably due to the structural difference between the two types of models. The semi-empirical models mostly employ two fixed piecewise functions, usually with harmonic and exponential curves, to depict daytime and nighttime LST dynamics, respectively. By comparison, a series of harmonic functions is added together and used to describe the diurnal LST dynamics. The less rigid functional forms of the quasi-physical models likely contribute to its greater flexibility in the nonstandard cases such that the LST may occasionally rise (or fluctuate) within the overall cooling trend subsequent to sunset (Huang et al., 2014), which is not uncommon for *in-situ* data because of microclimate variations. The results further illustrate that the performances of the two GEM-type models are generally similar, with overall RMSEs of 0.86 and 0.85 K for GEM-σ and GEM-η, respectively.

Under this case, we further observe that the GOT01-type models perform slightly better than the INA08-type ones, which is probably caused by the different cooling curves used by the two model types for nighttime. Closer investigation shows that the hyperbolic function used to represent nighttime cooling, when compared with the exponential function, is less capable of acquiring computationally stable solutions because hyperbolas are more sensitive to the predetermined initial values and small LST variations that are prevalent for *in-situ* LSTs. In addition, the PRA '$t_s = t_{ss} - 1$' is generally better than '$\delta T = 0$', although the associated RMSE variations frequently overlap (see Fig. 2). This behavior is also observed at nighttime and around sunrise (Fig. 3).

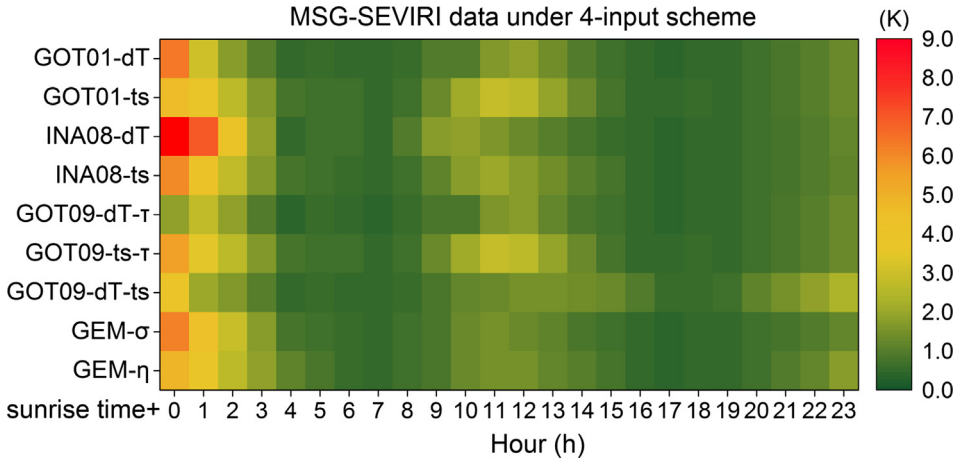

Fig. 9. Same as Fig. 7, but for the 4-input scheme.

4.2. Case #2: In-situ data under the 4-input scheme

Compared with the validations based on the 24-input scheme, the free parameters of the FPDs can be precisely determined by only four LST observations over a diurnal cycle (i.e., the 4-input scheme). This case is a good test of model stability and sensitivity as well as of its ability to predict an entire diurnal LST cycle when only four observations are available. The RMSEs of the nine models for an entire diurnal cycle as well as for the hourly errors are provided in Figs. 4 and 5, respectively. We found similarities using the 24- and 4-input schemes: (1) the GOT09- and GEM-type models continue to perform better than the other models; and (2) the relative performances of the three types of semi-empirical models remain similar, with the following decreasing order: GOT09-type models > GOT01-type models > INA08-type models.

However, we observed several differences between Cases #1 and 2:

First, the prediction capabilities of these models are reduced with the 4-input scheme when compared with the 24-input scheme, especially around sunrise (Figs. 3 and 5). The comparisons show that within this period, the mean RMSEs for the GOT09- and GEM-type models increase by approximately 1.0 K (from around 1.0 to 2.0 K), while those for the GOT01- and INA08-type models increase by approximately 5.0 K (from ~5.0 to 10.0 K). The significant decrease of model performance around sunrise can be partly attributed to the selection of the four observations close to the times of the four daily MODIS overpasses, i.e., no observation around sunrise has been used. This explains the decreased performance of the GEM- and GOT09-type models when the 4-input scheme was employed. We nevertheless infer that the neglect of the slow temperature increase around sunrise contributes more to the performance decrease of the GOT01- and INA08-type models, because the mean RMSEs of the GEM- and GOT09-type models remain relatively low around sunrise (Fig. 5).

Second, the prediction capabilities of the GEM-type models become lower than GOT09-dT-τ and GOT09-ts-τ, but slightly higher than GOT09-dT-ts, which differs from the highest capability of the GEM-type models as revealed under Case #1. The higher complexity of the GEM-type models by using harmonic series, as analyzed in Section 4.1, leads to their high performances for handling nonstandard cases under the 24-input scheme. However, such a high degree of complexity also results in a reduced robustness under the 4-input scheme.

Third, differing from the invariably better performance for the PRA '$t_s = t_{ss} - 1$' when compared with '$\delta T = 0$' as, shown in Fig. 2, the PRA fitness depends on the model type under Case #2. The box plots for the GOT01- and GOT09-type models in Fig. 4 indicate that '$\delta T = 0$' is at least equal to or superior than '$t_s = t_{ss} - 1$', while the former strategy is less effective than the latter for the INA08-type models, which was also confirmed by Duan et al. (2014b).

4.3. Case #3: Geostationary data under the 24-input scheme

Daily mean and hourly performance comparisons for the nine FPDs under the 24-input scheme with geostationary satellite data are shown in Figs. 6 and 7, respectively. Again, the performances of the original GOT01, INA08 and GOT09 models are added as references. Satellite-derived LSTs, when compared with the ground-based measurements, are less affected by the microclimate at the local scale, but they contain additional uncertainty from the LST retrieval algorithm (1.0–2.0 K, which is much higher than that of the *in-situ* LSTs). The results in Case #3 are similar to those under Case #1, such that the accuracies of the GOT01- and INA08-type models, on average, are lower than those of the GOT09-type models, which again can be attributed to the neglect of the slow LST increase after sunrise for the former two models (see Fig. 7). The results also resemble those under Case #2, e.g., GOT09-dT-τ possesses the highest accuracy in all FPDs and even performs better than the GOT01 and INA08 models. In addition, the accuracy losses caused by the use of PRAs remain small and may even become tiny in several cases (the accuracy losses are 0.13, 0.09, and 0.16 K for the GOT01-, INA08-, and GOT09-type models, respectively).

However, we have interpretations which differ from those of the previous two cases: First, in contrast to the significant contrast among models under Cases #1 and #2, the performances among different FPDs are much closer, with the highest daily mean RMSE of 1.56 K (for INA08-dT) and the lowest of 0.86 K (for GOT09-dT-τ). The relatively improved performances of the GOT01- and INA08-type models under Case #3 compared with those under Case #1 are probably caused by the fact that the temporal variations of the satellite-derived LSTs are smoother, since smoothness is an underlying assumption of all the DTC models. Second, the GO09-dT-τ performs considerably better than the other two GOT09-type models, including GOT09-ts-τ and GOT09-dT-ts, and it also performs better than the two GEM-type models (i.e., GEM-σ, and GEM-η). This result differs from that obtained under Case #1, where the GEM-type models performed better. As before, this can be explained by the temporally smoother satellite LSTs. The flexibility of the GEM-type models in handling nonstandard cases (e.g., a possible LST increase at night) makes it more unstable in standard cases (i.e., clear sky with no or low wind speed).

4.4. Case #4: Geostationary data under the 4-input scheme

Daily mean and hourly performances for the nine FPDs under the 4-input scheme with geostationary satellite data are shown in Figs. 8 and 9, respectively. Under this case, the model performances in decreasing order are: GOT09-dT-τ > GOT09-dT-ts > GOT01-dT > GOT01-ts > INA08-ts ≈ GOT09-ts-τ ≈ GEM-type models > INA08-dT (Fig. 8). The hourly RMSEs in Fig. 9 again suggest that this order of performance is directly related to the modelling ability to correctly reproduce the LST dynamics during the first 3–4 h after sunrise.

In contrast to the three previous cases, the assessments in Case #4 further reveal that the prediction capabilities of the GEM-type models greatly decrease, with the daily mean RMSEs marginally higher than 2.0 K (Fig. 7). The hourly assessments reveal that this is mainly due to the decreased performance around sunrise. Again, we infer that this is largely because of the high degree of complexity of this type of model which restricts their robustness with a small number of inputs. This may also partly be because the parametrization of the atmospheric transmittance attenuation by simply multiplying by $1–0.2\cdot(\cos Z)^{-0.5}$ is far from accurate (see Appendix B). Also differing from the assessments under Case #3, the PRA '$\delta T = 0$' is slightly better for the GOT01-type models under Case #4, while PRA '$t_s = t_{ss} - 1$' is slightly better under Case #3.

To illustrate the spatial variations of the prediction capabilities of the FPDs, we provide maps of daily mean RMSEs for GOT01-dT, INA08-dT, GOT09-dT-τ, and GEM-σ, each representing the model with the lowest prediction error within its own categories (Fig. 10). With hourly aggregated LSTs from FY-2F for January 2016 (not LSTs under a diurnally clear sky), Fig. 10 shows that the daily mean RMSE of the GOT09-dT-τ over a large part of mainland China is 1.48 K, which is about 0.3–0.4 K lower than for the other three models. The errors of GOT09-dT-τ are generally small (around 1.0 K) except over several small regions within the southern subtropical zone, where the errors of the other three models are also large. Close examination of the original data illustrates that over these regions the diurnal variations of the monthly mean LSTs are not as smooth as expected for LST dynamics under clear sky, and such fluctuated LST dynamics directly results in a relatively high error for all FPDs. Note that the southwest-toward-northeast boundaries, across which the RMSEs change abruptly, are caused by anomalies in the original LST product.

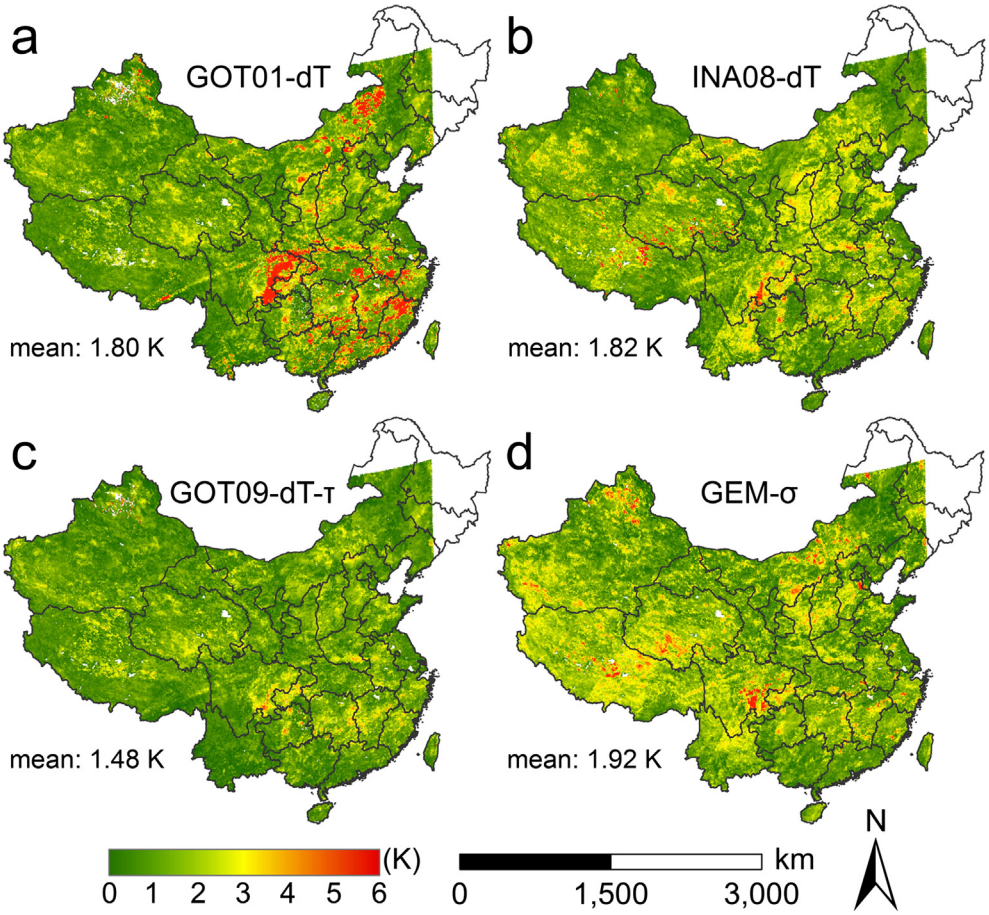

Fig. 10. Spatial variations of the daily mean RMSEs for the four FPDs under the 4-input validation scheme. (a) GOT01-dT, (b) INA08-dT, (c) GOT09-dT-τ, and (d) GEM-σ.

5. Discussion

5.1. Optimal value of τ for GOT09-type models

To reduce the number of parameters of the DTC models to four, it is sometimes necessary to fix some of the free parameters. The aforementioned evaluations on the GOT09-type models indicate that most of the predicted LST errors occurring shortly after sunrise can be compensated (with only a very small loss of accuracy) by setting TOT (τ) to a constant. To obtain a representative and optimal value of τ for various cases, including dissimilar land cover types and background climates, we tested a series of τ values ranging from 0.0 to 0.2, which covers most practical situations, and identified the best one according to the achieved accuracy. The error, as a function of τ for both the *in-situ* and geostationary LSTs under the 24- and 4-input schemes, is shown in Fig. 11.

The results in Fig. 11 confirm the previous assessment that GOT09-dT-τ performs better than GOT09-ts-τ, and the superior performance of the former model generally becomes more pronounced as τ increases. The only exception occurs under the 24-input scheme with a low τ value, for which GOT09-ts-τ is slightly better (Fig. 11a and b). In general, the RMSEs of the GOT09-type models follow a decreasing and then an increasing trend. Typically, they decrease rapidly when τ changes from 0.0 to a value marginally greater than zero (e.g., 0.003 or 0.01), and gradually increase when τ continues to increase. For the *in-situ* and SEVIRI LSTs, the RMSEs vary considerably with τ and they cover a range of about 1.0 K; while the RMSE variations for the VISSR LSTs are considerably smaller with a maximum change of about 0.3 K. More specifically, the optimal τ is 0.01 and 0.003 for the 4- and 24-input schemes with *in-situ* LSTs (Fig. 11a). With SEVIRI LSTs, the optimal value remains at 0.01 for the GOT09-dT-τ, but decreases (i.e., 0.001) for GOT09-ts-τ (Fig. 11b). Based on VISSR LSTs, its optimal value is likewise relatively low (i.e., 0.002–0.005) for GOT09-ts-τ, but it increases significantly to around 0.02–0.06 for GOT09-dT-τ (Fig. 11c). We infer that the difference in terms of determining the optimal value of τ using the VISSR LSTs, compared with using the two other types of LSTs, is probably because temporally aggregated LSTs, rather than LSTs under a true clear sky, were used for the VISSR data.

In summary, by considering these different cases as a whole, setting τ to 0.01 appears to be an acceptable tradeoff. Though the setting of τ as a constant (0.01) may not be optimal for all cases, this value is generally an acceptable tradeoff because (1) it is close to the optimal value of τ determined under different cases and (2) RMSE differences between the best τ and 0.01 under many different cases are negligible. Note that although the optimal value of τ (0.01) was determined using data from multiple cases, the optimal value of τ for the 4- or 24-input schemes may differ from the true TOT. This is because the accurate determination of τ is most sensitive to the LST observations shortly after sunrise, while there are only approximately 1–3 LST observations as inputs, even for the 24-input scheme. In other words, once abundant LST observations over an entire diurnal cycle (but very few for shortly after sunrise) are available, the value of τ resolved by numerical methods (i.e., nonlinear fitting) would probably contain additional information on LST dynamics in addition to the physical TOT. The determined value of τ, therefore, becomes inconsistent with the true TOT. To estimate TOT precisely, temporally denser data (e.g., 5- or 15-min LSTs) are needed to ensure that an adequate number of LST observations is accessible during the short period after sunrise, as used by Göttsche and Olesen (2009).

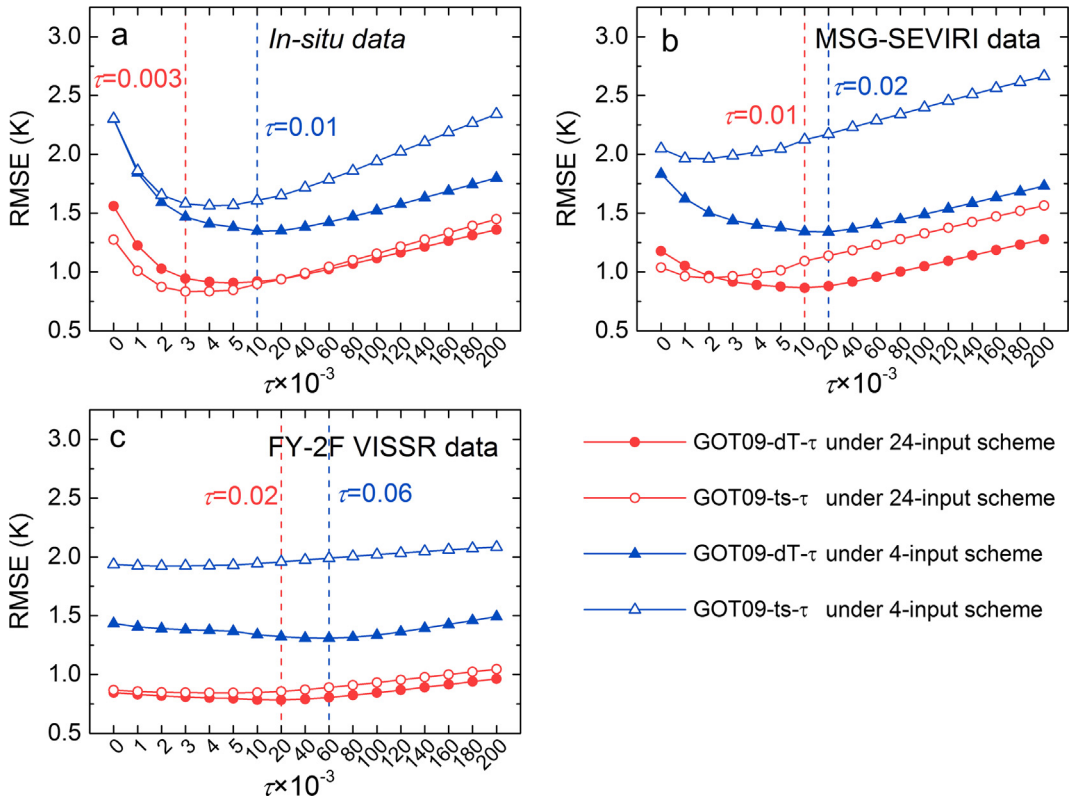

Fig. 11. Errors of two GOT09-type models as a function of τ when provided with 4 and 24 input LSTs: (a) *in-situ* data, (b) LSA SAF LST derived from MSG-SEVIRI, and (c) LST derived from FY-2F VISSR.

5.2. Uncertainty discussions for geostationary satellite-derived LST

Due to the uncertainties in atmospheric water vapor estimate and emissivity determination, which are typically required inputs of LST retrieval algorithms (Wan and Li, 1997; Freitas et al. 2010). LST products derived from geostationary satellites possess an uncertainty of 1.0–2.0 K (refer to the descriptions on QC flags given in Section 2.2), which may affect the relative performance of the nine investigated nine FPDs. Usually, retrieval errors from satellite-derived LSTs can be divided into systematic biases and random errors. Previous investigations have clarified that systematic biases (systematically higher or lower) hardly influence FPD performances (Duan et al., 2012). Our results using temporally aggregated LST data (monthly FY-2F LST composites), by which random errors could be mostly eliminated and only systematic biases were left, also elucidate that GOT09-dT-τ remains the best FPDs among the nine FPDs.

To test the impact of random errors on FPD performances, we added a series of random errors to the original SEVIRI LSTs, which were assumed to be error-free. Note that (1) these added random errors follow the Gaussian distribution, with 0.0 and 1.0 K as the associated mean and standard deviation (STD), respectively; (2) each diurnal cycle was re-modelled 50 times, obtaining a total of 5550 diurnal cycles fitted diurnal cycles (111 cycles × 50 = 5550 cycles). Based on these results, the FPD performances were re-evaluated. Fig. 12 shows RMSE boxplots corresponding to the investigated FPDs under 24-input and 4-input schemes. Compared with the previous results (refer to Figs. 6 and 8), the RMSEs shows in Fig. 12 are greater, which is reasonable because random errors have been added. Nevertheless, the performance order of FPDs remain nearly identical as before. These assessments suggest that the relative performance of the FPDs is insensitive to the LST retrieval errors (i.e., quality controls).

5.3. On the impacts from seasonality, land cover type, and topographic characteristic on order of model performance

Previous studies primarily analyzed RMSE's mean and its spread, indicating that the identified FPD may not always be the optimal under various cases. In particular, it remains unclear whether or not factors including seasonality, land cover type, and topographic characteristic (here we only consider elevation) significantly influence the performance of the models. In order to test the sensitivity of the order of model performance to these factors, we further investigated FPD performances stratified by seasonality, land cover type, and elevation (Fig. 13).

The results show that the previously drawn conclusions are still valid, namely that (1) the GEM-type models perform excellently for *in-situ* measurements under 24-input scheme, while (2) the GOT09-type models are most suitable for the other three cases (Fig. 13). However, we observe some exceptions in terms of the investigated factors. For example, the assessments indicate that GEM-η performs better than GOT09-dT-τ during spring (subplot a3), while INA08-ts is similarly identified as the best in autumn and winter (subplot a3). When investigating the dependence on land cover type, GEM-η surpasses GOT09-dT-τ over the mixed cover type E (subplot b3). GEM-η also performs best over surfaces with elevations greater than 1200 m (subplots c3 and c4). It is difficult to isolate the specific reason for these exceptions, but the surface thermal properties (related to land cover type and soil moisture), synoptic conditions, and errors in measurements or retrievals of LSTs are expected playing important roles altogether on provoking these exceptions.

From these assessments, as well as those in Section 4, it is inferred that the overall performance of a model is primarily determined by its performance around sunrise, which is considered in particular in the design of the GEM- and GOT09-type models. Furthermore, the order of model performance is fairly insensitive to the factors such as the

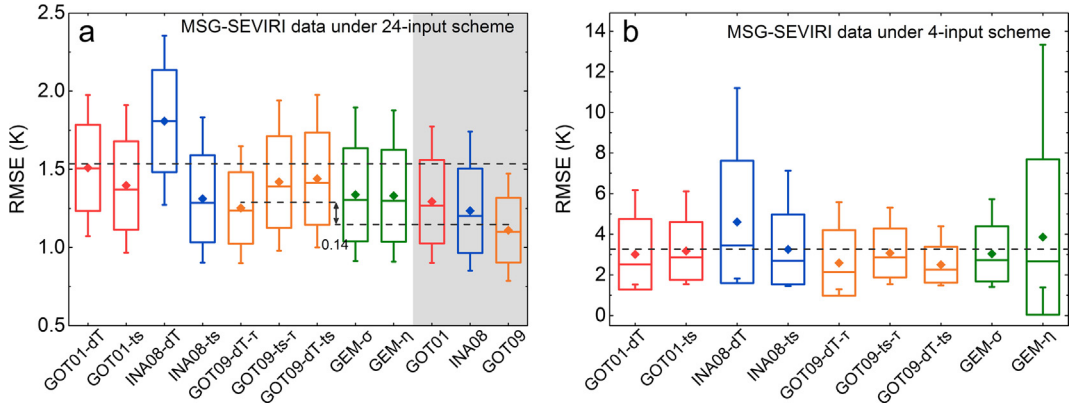

Fig. 12. Boxplots of the overall RMSEs for all the FPDs with disturbed (Gaussian noise added) MSG-SEVIRI LSTs under 24-input and 4-input schemes: (a) same as Fig. 2, but for the disturbed MSG-SEVIRI LSTs; (b) same as Fig. 4, but for the disturbed MSG-SEVIRI LSTs.

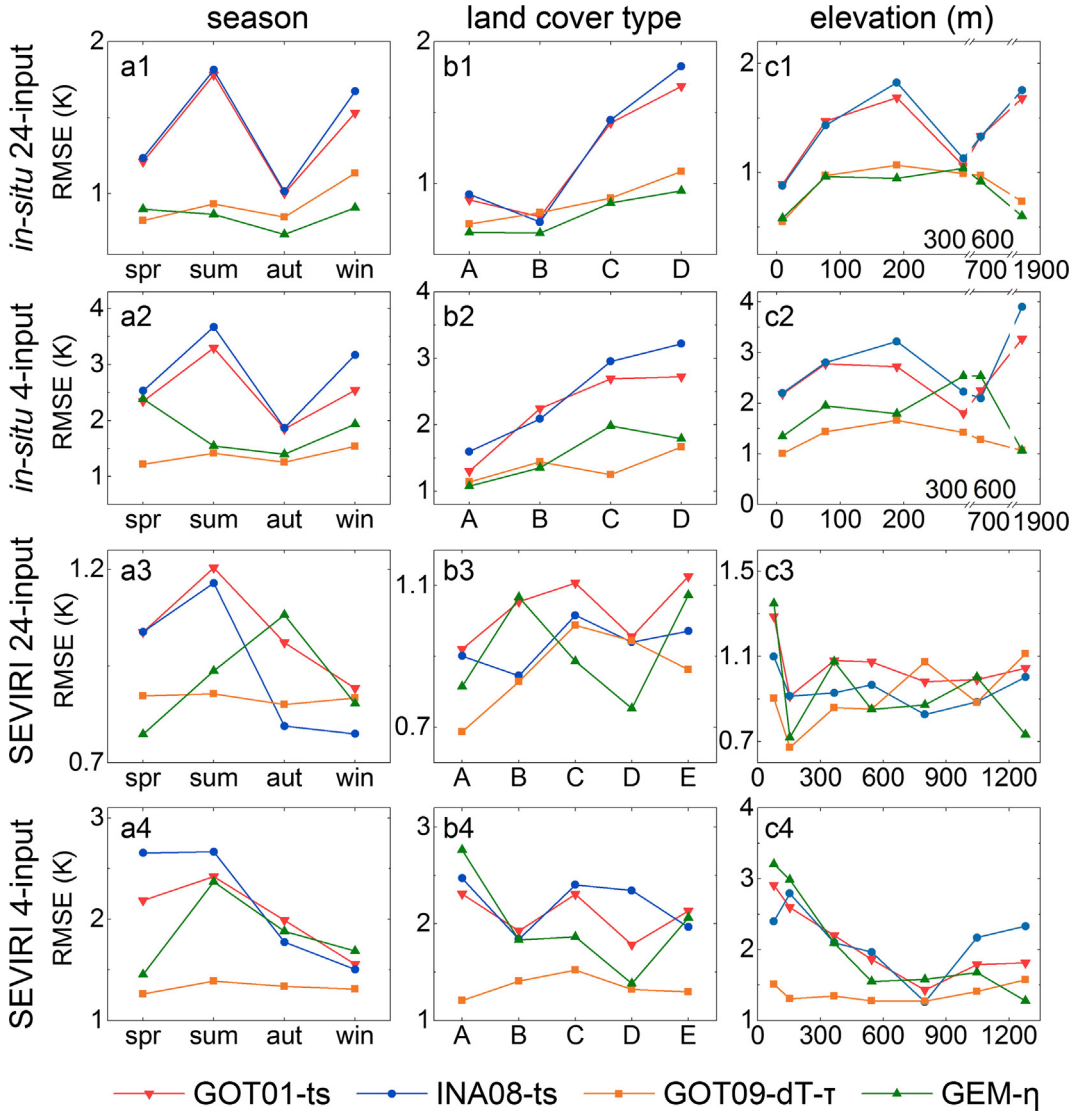

Fig. 13. Performance variations of FPDs depending on input dataset and input scheme (see row labelling). The columns show the dependence on season (first column), land cover type (second column), and elevation (third column). Note that only results for the better/best sub-model among the associated model types are shown, i.e. GOT01-ts, INA08-ts, GOT09-dT-τ, and GEM-η, respectively. For *in-situ* measurements, the investigated land cover types are tree (A), shrub (B), grass (C), and bare soil (D), while for SEVIRI LSTs, the land cover types are closed shrublands (A), open shrublands (B), croplands (C), mix of wood savannas, savannas and grasslands (D), and barren or sparely vegetated surfaces (E).

Table 5
Orders of parameter-reduction strategies for each type of DTC model, summaries of the features for each model type, and recommended model(s) under different cases.

Cases	GOT01*	INA08	GOT09	GEM	Recommended model
Case #1	$t_s > \delta T$	$t_s > \delta T$	$\tau \approx t_s > \delta T$	$\sigma \approx \eta_1$	*GEM and GOT09 types*
Case #2	$\delta T \approx t_s$	$t_s > \delta T$	$\tau > \delta T > t_s$	$\sigma > \eta_1$	*GOT09 type*
Case #3	$t_s > \delta T$	$t_s > \delta T$	$\delta T \approx \tau > t_s$	$\eta_1 \approx \sigma$	*GOT09 type*
Case #4	$\delta T > t_s$	$t_s > \delta T$	$\delta T > \tau > t_s$	$\eta_1 > \sigma$	*GOT09 type*
Summary	● *simple form* ● *less capability around sunrise*	● *simple form* ● *less capability around sunrise*	● *relatively complex form* ● *high accuracy*	● *complex form* ● *suitable for nonstandard and adequate-input cases*	*GOT09 type*

* 'δT', 't_s', 'τ', 'σ', 'η_1' denote the five PRAs including '$\delta T = 0$', '$t_s = t_{ss} - 1$', '$\tau = 0.01$', '$\sigma = 0$', and '$\eta_1 = 0$', respectively. The symbol ' > ' means that the left parameter reduction strategy has a better performance than the one on the right, while the symbol '≈' indicates a similar performance.

seasonality, land cover type, and elevation, although the result demonstrate that these factors affect the absolute errors of the investigated FPDs.

5.4. Summaries of selection PRAs and the outlook for DTC models with different numbers of parameters

Based on the results presented above, we find that the performances of the FPDs are primarily determined by the original model type and the loss of accuracy caused by different PRAs; while they are relatively less impacted by surface regulators such as the season and land cover type. Therefore, we further provide the orders of the parameter-reduction strategies for each investigated category of DTC model, the features for each model type, as well as the recommended model(s) under various cases (see Table 5). For example, the order '$\delta T > \tau > t_s$' for the GOT09 model under Case #4 means that the optimal strategy to reduce the parameter number to four is to set δT to zero at first and subsequently τ to 0.01. Furthermore, the results in Table 5 suggest that the parameter number can be reduced to three by adding the PRA '$t_s = t_{ss} - 1$'. However, it should be noted that accuracy decreases when only three free parameters are used.

Moreover, to conduct DTC modeling when only two observations are available (e.g., between 2000 and 2002, only MODIS observations from Terra are available), for semi-empirical models, one can further reduce the parameter number by fixing t_m as a constant according to the timing results for different land-cover types obtained by Holmes et al. (2013) and Good et al. (2017). For quasi-physical models, one can use an approach similar to that of Watson (2000) and Huang et al. (2014) by only retaining two parameters, such as thermal inertia (P) and daily mean LST (T_0).

However, we need to clarify that the errors of the DTC models with only two free parameters would be probably greater than the FPDs. One possible solution is to additionally integrate data from other sources. These data can be the aerosol optical depth (AOD) products provided by MODIS, which offer potentially useful information for determining τ. The problem of limited daily thermal observations can also be solved by integrating background diurnal LST dynamics at lower resolutions, such as the geostationary-satellite-based diurnal dynamics (Sun and Pinker, 2005; Zhou et al., 2013) or land-surface-model-based LST dynamics (Jin and Dickinson, 1999). Information on land cover types and surface properties (e.g., NDVI) is also valuable for DTC modeling when limited diurnal thermal observations are available (Quan et al., 2014). Finally, due to the similar diurnal variation patterns between LST and air temperature, the ground-based air temperatures can also be useful for DTC modeling with limited observations (Bechtel et al., 2014, 2017; Ignatov and Gutman, 1999; Xue and Cracknell, 1995; Zakšek and Schroedter-Homscheidt, 2009; Zhu et al., 2017).

Previous performance assessments of FPDs were mainly conducted under clear-sky conditions. Nevertheless, clouds are prevalent for most of the earth surfaces especially at low latitudes, which result in invalid thermal observations of surfaces. Therefore, there is frequently an inadequate number of LSTs (i.e., less than four) available for FPD modelling. This dilemma can be solved, as indicated, by either further fixing some of the parameters of the FPDs or by integrating auxiliary data such as surface air temperatures and radiation measurements (Jin and Dickinson, 1999; Lu et al., 2011; Zhang et al., 2015). However, strictly speaking, the parametric DTC models investigated here are only valid under clear-sky condition. Therefore, in the presence of frequent clouds, a feasible solution is to temporally aggregate the clear-sky MODIS LSTs at each observation daily time over a certain number of days (e.g., 8 days, a month or a season) to obtain representative clear-sky LST, as those performed for the FY-2F data in Section 4.4. Though the modeling of temporally aggregated LSTs cycles does not provide the LST dynamics of a specific day, it is potentially useful in various applications focusing on the more slowly varying thermal characteristics of the land surface rather than individual LSTs, such as the derivation of the diurnal dynamics of surface UHIs (Zakšek & Oštir, 2012) and temporal upscaling of instantaneous surface evapotranspiration. Finally, one should be aware that even if four thermal observations per day (e.g., four MODIS LSTs) were obtained under clear-sky conditions, clouds may still have occurred at any other time of the diurnal cycle. Therefore, the corresponding modelled LSTs at these times will not necessarily reflect actual LSTs. Under this condition, the modelled LSTs by FPDs would be probably greater for the day while lower for the night, because daytime clouds can block direct solar radiation while nighttime clouds can produce atmospheric counter radiation that keep the surface relatively warmer.

6. Conclusions

Four-parameter DTC models (FPDs) are crucial to various applications, but until now a systematic comparison among the commonly used FPDs has not been performed. This study aims at summarizing all the possible FPDs with different parameter-reduction approaches (PRAs) and further identifying the FPDs with the highest accuracy under various cases. Both *in-situ* and geostationary LST data over extensive areas under dissimilar bioclimates were used for comparison.

Our findings are as follows: (1) Prediction accuracy within the period shortly after sunrise determines a large part of the daily mean modelling accuracy, but it rarely affects the accuracy in the afternoon. (2) For the GOT01- type models, PRA '$\delta T = 0$' is less accurate than '$t_s = t_{ss} - 1$' under 24-input scheme, but slightly better under 4-input scheme. For the INA08-type models, PRA '$\delta T = 0$' is less accurate than '$t_s = t_{ss} - 1$', but the first strategy generally yields better results for GOT09-type models. (3) The GOT09- and GEM-type models are recommended when hourly or more frequent thermal observations are available. The GEM-type models are only recommended in nonstandard cases (e.g., the LSTs fluctuate and even increase slightly rise during the nighttime cooling period), while the GOT09-type models are generally the optimal option for typical uses. (4) Among the three GOT09-type models, GOT09-dT-τ (for which δT and τ are fixed to zero and 0.01, respectively) usually performs better than the other two models (i.e.,

GOT09-ts-τ and GOT09-dT-ts). Therefore, GOT09-dT-τ is further identified as the most suitable option for general use in various applications. These findings are potentially useful for the retrieval of surface thermal properties as well as for the generation of spatio-temporally continuous LSTs that are required for various applications, such as the generation of surface air temperatures at high resolution, thermal remote sensing of evapotranspiration, and urban heat islands.

Acknowledgements

We gratefully acknowledge the U.S. Climate Reference Network (USCRN), the Satellite Application Facility (SAF) on Land Surface Analysis (LSA), a project funded by the European Organisation for the Exploitation of Meteorological Satellites (EUMETSAT), and the China Meteorological Administration National Satellite Meteorological Center (CMA NSMC) for providing the *in-situ* and geostationary thermal observations.

This work is jointly supported by the Key Research and Development Programs for Global Change and Adaptation under Grant number 2016YFA0600201, the National Natural Science Foundation of China under Grant number 41671420, the Key Research and Development Programs for Global Change and Adaptation under Grant number 2017YFA0603604, the Fundamental Research Funds for the Central Universities under Grant number 090414380017, and the Ministry Science and Technology Development of China-Data Sharing Infrastructure of Earth System Science under Grant number 2005DKA32300. We are grateful for the DengFeng Program-B of Nanjing University.

Appendix A. Performance comparison between using two different parameter-reduction approaches on determining t_s

Here, we compare two different parameter-reduction approaches (PRAs) for t_s. The two PRAs are provided by the following formula (Duan et al., 2014b; Holmes et al., 2013):

$$\begin{cases} t_s = p_1(t_{ss}) = t_{ss} - 1 \\ t_s = p_2(t_m, T_a, \delta T) = t_m + \omega\pi^{-1}\arccos[0.5\cdot(1 + \delta T\cdot T_a^{-1})] \end{cases} \tag{A1}$$

where p_1 and p_2 represent these two PRAs; t_{ss} is time of sunset; and t_m, T_a, and δT are the time when LST reaches its maximum, daily LST amplitude, and temperature difference between T_0 and $T(t\to\infty)$, respectively. The associated assessments for these two PRAs (see Table A1) show that p_1 is less capable than p_2 only in four of the sixteen cases, including GOT01-ts and INA08-ts under Case #1, GOT09-dT-ts under Case #3 and #4. For the rest of the listed cases, p_1 yields a higher accuracy.

Table A1
Performances of the two PRAs given by Eq. (A1). Only four-parameter DTC models (i.e., GOT01-ts, INA08-ts, GOT09-ts-τ, and GOT09-dT-ts) that include parameter t_s are compared.

Case*	GOT01-ts**	INA08-ts	GOT09-ts-τ	GOT09-dT-ts
Case #1	$p_1 < p_2$	$p_1 < p_2$	$p_1 > p_2$	$p_1 > p_2$
Case #2	$p_1 > p_2$	$p_1 > p_2$	$p_1 > p_2$	$p_1 > p_2$
Case #3	$p_1 > p_2$	$p_1 > p_2$	$p_1 \approx p_2$	$p_1 < p_2$
Case #4	$p_1 > p_2$	$p_1 > p_2$	$p_1 > p_2$	$p_1 < p_2$

* Cases #1 to #4 denote the four validation schemes given in Section 3.3.

** '$p_1 < p_2$' indicates that PRA p_1 is less efficient than p_2, while '$p_1 > p_2$' denotes the opposite.

Appendix B. Formula for calculating M_n and $g(t)$

For the GEM models mentioned in Section 3.1.3, M_n and $g(t)$ are written as follows (Huang et al., 2014):

$$\begin{cases} M_n = [n\omega_d P^2 + \sqrt{2n\omega_d}P\cdot h_1 + h_1]^{-1/2} \\ g(t) = A_n\cos(n\omega_d - \phi_n) + B_n\sin(n\omega_d - \phi_n) \\ \phi_n = \arctan[P\sqrt{n\omega_d}\cdot(\sqrt{2}h_0 + P\sqrt{n\omega_d})^{-1}] \end{cases} \tag{B1}$$

where n denotes the number of items of the Fourier series (it approaches infinity in theory but it can be set to 10 for simple uses); ω_d is the angular velocity of the earth; ϕ_n is an intermediate function; P denotes the thermal inertia; h_1 and h_0 are respectively the linear and constant coefficients of the upward surface fluxes; and A_n and B_n are the Fourier coefficients at the n^{th} order, expressed as:

$$\begin{cases} A_n = (2\pi)^{-1}\int\limits_{\omega_d t\in W} f(\omega_d t)\cos(n\omega_d t)d\omega_d t \\ B_n = (2\pi)^{-1}\int\limits_{\omega_d t\in W} f(\omega_d t)\sin(n\omega_d t)d\omega_d t \end{cases} \tag{B2}$$

where $f(t)$ is the solar radiation received by the surface within a diurnal cycle. It is a piecewise function that takes the cosine value of a solar zenith angle of 0.04 as the dividing point to distinguish the daytime and nighttime periods (Watson, 1975).

The function $f(t)$ is expressed as the following for the daytime period:

$$\begin{cases} f(t) = (1-\alpha)\cdot S_0\cdot\cos Z\cdot\kappa \\ \omega_d t \in W_{sunlit} = [0, 2\pi]\cap\{\cos Z > 0.04\} \end{cases} \tag{B3}$$

where α is the surface albedo; S_0 is the solar constant (1367 W/m^{-2}); and Z, κ, and W_{sunlit} are the solar zenith angle, atmospheric transmittance, and the daytime period with solar insolation, respectively. Z and κ are calculated using the formula:

$$\begin{cases} \cos Z = \cos\delta\cos\varphi\cos\omega_d t + \sin\delta\sin\varphi \\ \kappa = 1-0.2\sqrt{\sec Z} \end{cases} \quad \text{(B4)}$$

where δ and φ are the solar declination and local latitude, respectively.
The function $f(t)$ is expressed as follows for the nighttime period:

$$\begin{cases} f(t) = 0 \\ \omega_d t \in W_{\text{shaded}} = [0,\ 2\pi] \cap \{\cos Z \leqslant 0.04\} \end{cases} \quad \text{(B5)}$$

where W_{shaded} is the period without solar radiation.

References

Aires, F., Prigent, C., Rossow, W.B., 2004. Temporal interpolation of global surface skin temperature diurnal cycle over land under clear and cloudy conditions. J. Geophys. Res. 109, D04313. http://dx.doi.org/10.1029/2003JD003527.

Anderson, M.C., Norman, J.M., Kustas, W.P., Houborg, R., Starks, P.J., Agam, N., 2008. A thermal-based remote sensing technique for routine mapping of land-surface carbon, water and energy fluxes from field to regional scales. Remote Sens. Environ. 112 (12), 4227–4241. http://dx.doi.org/10.1016/j.rse.2008.07.009.

Bechtel, B., Wiesner, S., Zakšek, K., 2014. Estimation of dense time series of urban air temperatures from multitemporal geostationary satellite data. IEEE J. Sel. Top. Appl. Earth Obs. Remote Sens. 7 (10), 4129–4137. http://dx.doi.org/10.1109/JSTARS.2014.2322449.

Bechtel, B., Zakšek, K., Oßenbrügge, J., Kaveckis, G., Böhner, J., 2017. Towards a satellite based monitoring of urban air temperatures. Sustain. Cities Soc. 34, 22–31. http://dx.doi.org/10.1016/j.scs.2017.05.018.

Cracknell, A.P., Xue, Y., 1996. Dynamic aspects study of surface temperature firom remotely-sensed data using advanced thermal inertia model. Int. J. Remote Sens. 17 (13), 2517–2532. http://dx.doi.org/10.1080/01431169608949090.

Duan, S.B., Li, Z.L., Tang, B.H., Wu, H., Tang, R., 2014a. Generation of a time-consistent land surface temperature product from MODIS data. Remote Sens. Environ. 140, 339–349. http://dx.doi.org/10.1016/j.rse.2013.09.003.

Duan, S.B., Li, Z.L., Tang, B.H., Wu, H., Tang, R., Bi, Y., Zhou, G., 2014b. Estimation of diurnal cycle of land surface temperature at high temporal and spatial resolution from clear-sky MODIS data. Remote Sens. 6 (4), 3247–3262. http://dx.doi.org/10.3390/rs6043247.

Duan, S.B., Li, Z.L., Wang, N., Wu, H., Tang, B.H., 2012. Evaluation of six land-surface diurnal temperature cycle models using clear-sky in situ and satellite data. Remote Sens. Environ. 124 (2), 15–25. http://dx.doi.org/10.1016/j.rse.2012.04.016.

Duan, S.B., Li, Z.L., Wu, H., Tang, B.H., Jiang, X., Zhou, G., 2013. Modeling of day-to-day temporal progression of clear-sky land surface temperature. IEEE Geosci. Remote Sens. Lett. 10 (5), 1050–1054. http://dx.doi.org/10.1109/LGRS.2012.2228465.

Freitas, S.C., Trigo, I.F., Bioucas-Dias, J.M., Göttsche, F.M., 2010. Quantifying the uncertainty of land surface temperature retrievals from SEVIRI/Meteosat. IEEE Trans. Geosci. Remote Sens. 48 (1), 523–534. http://dx.doi.org/10.1109/TGRS.2009.2027697.

Friedl, M.A., McIver, D.K., Hodges, J.C.F., Zhang, X.Y., Muchoney, D., Strahler, A.H., Woodcock, C.E., Gopal, S., Schneider, A., Cooper, A., Baccini, A., Gao, F., Schaaf, C., 2002. Global land cover mapping from MODIS: algorithms and early results. Remote Sens. Environ. 83 (1), 287–302. http://dx.doi.org/10.1016/S0034-4257(02)00078-0.

Göttsche, F.M., Olesen, F.S., 2001. Modelling of diurnal cycles of brightness temperature extracted from meteosat data. Remote Sens. Environ. 76 (3), 337–348. http://dx.doi.org/10.1016/S0034-4257(00)00214-5.

Göttsche, F.M., Olesen, F.S., 2009. Modelling the effect of optical thickness on diurnal cycles of land surface temperature. Remote Sens. Environ. 113 (11), 2306–2316. http://dx.doi.org/10.1016/j.rse.2009.06.006.

Göttsche, F.M., Olesen, F.S., Trigo, I.F., Bork-Unkelbach, A., Martin, M.A., 2016. Long term validation of land surface temperature retrieved from MSG/SEVIRI with continuous in-situ measurements in Africa. Remote Sens. 8 (5). http://dx.doi.org/10.3390/rs8050410.

Gholamnia, M., Alavipanah, S.K., Boloorani, A.D., Hamzeh, S., Kiavarz, M., 2017. Diurnal air temperature modeling based on the land surface temperature. Remote Sens. 9 (9). http://dx.doi.org/10.3390/rs9090915.

Good, E.J., Ghent, D.J., Bulgin, C.E., Remedios, J.J., 2017. A spatiotemporal analysis of the relationship between near-surface air temperature and satellite land surface temperatures using 17 years of data from the ATSR series. J. Geophys. Res. Atmos. 122 (17), 9185–9210. http://dx.doi.org/10.1002/2017JD026880.

Hain, C.R., Anderson, M.C., 2017. Estimating morning change in land surface temperature from MODIS day/night observations: applications for surface energy balance modeling. Geophys. Res. Lett. 44 (19), 9723–9733. http://dx.doi.org/10.1002/2017GL074952.

Holmes, T.R.H., Crow, W.T., Hain, C., 2013. Spatial patterns in timing of the diurnal temperature cycle. Hydrol. Earth Syst. Sci. 17 (10), 3695–3706. http://dx.doi.org/10.5194/hess-17-3695-2013.

Holmes, T.R.H., Crow, W.T., Hain, C., Anderson, M.C., Kustas, W.P., 2015. Diurnal temperature cycle as observed by thermal infrared and microwave radiometers. Remote Sens. Environ. 158, 110–125. http://dx.doi.org/10.1016/j.rse.2014.10.031.

Holmes, T.R.H., Hain, C.R., Anderson, M.C., Crow, W.T., 2016. Cloud tolerance of remote-sensing technologies to measure land surface temperature. Hydrol. Earth Syst. Sci. 20 (8), 3263–3275. http://dx.doi.org/10.5194/hess-20-3263-2016.

Huang, F., Zhan, W., Duan, S.B., Ju, W., Quan, J., 2014. A generic framework for modeling diurnal land surface temperatures with remotely sensed thermal observations under clear sky. Remote Sens. Environ. 150 (7), 140–151. http://dx.doi.org/10.1016/j.rse.2014.04.022.

Ignatov, A., Gutman, G., 1999. Monthly mean diurnal cycles in surface temperatures over land for global climate studies. J. Clim. 12 (7), 1900–1910. http://dx.doi.org/10.1175/1520-0442(1999) 012<1900:MMDCIS>2.0.CO;2.

Imhoff, M.L., Zhang, P., Wolfe, R.E., Bounoua, L., 2010. Remote sensing of the urban heat island effect across biomes in the continental USA. Remote Sens. Environ. 114 (3), 504–513. http://dx.doi.org/10.1016/j.rse.2009.10.008.

Inamdar, A.K., French, A., Hook, S., Vaughan, G., Luckett, W., 2008. Land surface temperature retrieval at high spatial and temporal resolutions over the southwestern United States. J. Geophys. Res. Atmos. 113 (D7), 1829–1836. http://dx.doi.org/10.1029/2007JD009048.

Jiang, G.M., Li, Z.L., Nerry, F., 2006. Land surface emissivity retrieval from combined mid-infrared and thermal infrared data of MSG-SEVIRI. Remote Sens. Environ. 105 (4), 326–340. http://dx.doi.org/10.1016/j.rse.2006.07.015.

Jin, M., Dickinson, R.E., 1999. Interpolation of surface radiative temperature measured from polar orbiting satellites to a diurnal cycle 1. Without clouds. J. Geophys. Res. Atmos. 104 (D2), 2105–2116. http://dx.doi.org/10.1029/1998JD200005.

Karnieli, A., Agam, N., Pinker, R.T., Anderson, M., Imhoff, M.L., Gutman, G.G., Panov, N., Goldberg, A., 2010. Use of NDVI and land surface temperature for drought assessment: merits and limitations. J. Clim. 23 (3), 618–633. http://dx.doi.org/10.1175/2009JCLI2900.1.

Liu, Z., Wu, P., Duan, S., Zhan, W., Ma, X., Wu, Y., 2017. Spatiotemporal Reconstruction of land surface temperature derived from FengYun geostationary satellite data. IEEE J. Sel. Top. Appl. Earth Obs. Remote Sens. 10 (10), 4531–4543. http://dx.doi.org/10.1109/JSTARS.2017.2716376.

Lu, L., Venus, V., Skidmore, A., Wang, T., Luo, G., 2011. Estimating land-surface temperature under clouds using MSG/SEVIRI observations. Int. J. Appl. Earth Obs. Geoinf. 13 (2), 265–276. http://dx.doi.org/10.1016/j.jag.2010.12.007.

Parton, W.J., Logan, J.A., 1981. A model for diurnal variation in soil and air temperature. Agric. Met. 23 (84), 205–216. http://dx.doi.org/10.1016/0002-1571(81)90105-9.

Price, J.C., 1977. Thermal inertia mapping: a new view of the Earth. J. Geophys. Res. 82 (18), 2582–2590. http://dx.doi.org/10.1029/JC082i018p02582.

Qiao, Z., Tian, G., Xiao, L., 2013. Diurnal and seasonal impacts of urbanization on the urban thermal environment: a case study of Beijing using MODIS data. ISPRS J. Photogramm. Remote Sens. 85, 93–101. http://dx.doi.org/10.1016/j.isprsjprs.2013.08.010.

Quan, J., Chen, Y., Zhan, W., Wang, J., Voogt, J., Li, J., 2014. A hybrid method combining neighborhood information from satellite data with modeled diurnal temperature cycles over consecutive days. Remote Sens. Environ. 155, 257–274. http://dx.doi.org/10.1016/j.rse.2014.08.034.

Schädlich, S., Göttsche, F.M., Olesen, F.S., 2001. Influence of land surface parameters and atmosphere on METEOSAT brightness temperatures and generation of land surface temperature maps by temporally and spatially interpolating atmospheric correction. Remote Sens. Environ. 75 (1), 39–46. http://dx.doi.org/10.1016/S0034-4257(00)00154-1.

Sobrino, J.A., El Kharraz, M.H., 1999. Combining afternoon and morning NOAA satellites for thermal inertia estimation. 1. Algorithm and its testing with Hydrologic Atmospheric Pilot Experiment-Sahel data. J. Geophys. Res. Atmos. 104 (D8), 9445–9453. http://dx.doi.org/10.1029/1998JD200109.

Sun, D., Pinker, R.T., 2005. Implementation of GOES-based land surface temperature diurnal cycle to AVHRR. Int. J. Remote Sens. 26 (18), 3975–3984. http://dx.doi.org/10.1080/01431160500117634.

Tang, B., Bi, Y., Li, Z.A., Xia, J., 2008. Generalized split-window algorithm for estimate of land surface temperature from Chinese geostationary FengYun meteorological satellite (FY-2C) data. Sensors 8 (2), 933–951. http://dx.doi.org/10.3390/s8020933.

Trigo, I.F., Dacamara, C.C., Viterbo, P., Roujean, J.L., Olesen, F., Barroso, C., Camacho-De-Coca, F., Carrer, D., Freitas, S.C., García-Haroj, J., Geiger, B., Gellens-Meulenberghs, F., Ghilain, N., Meliá, J., Pessanha, L., Siljamo, N., Arboleda, A., 2011. The satellite application facility for land surface analysis. Int. J. Remote Sens. 32 (10), 2725–2744. http://dx.doi.org/10.1080/01431161003743199.

Van Den Bergh, F., Van Wyk, M.A., Van Wyk, B.J., Udahemuka, G., 2007. A comparison of data-driven and model-driven approaches to brightness temperature diurnal cycle interpolation. S. Afr. Inst. Electr. Eng. 98 (3), 81–86.

Vancutsem, C., Ceccato, P., Dinku, T., Connor, S.J., 2010. Evaluation of MODIS land surface temperature data to estimate air temperature in different ecosystems over Africa. Remote Sens. Environ. 114 (2), 449–465. http://dx.doi.org/10.1016/j.rse.2009.10.002.

Wan, Z., Li, Z.L., 1997. A physics-based algorithm for retrieving land-surface emissivity

and temperature from EOD/MODIS data. IEEE Trans. Geosci. Remote Sens. 35 (4), 980–996. http://dx.doi.org/10.1109/36.602541.
Wan, Z., Wang, P., Li, X., 2004. Using MODIS land surface temperature and normalized difference vegetation index products for monitoring drought in the southern Great Plains, USA. Int. J. Remote Sens. 25 (1), 61–72. http://dx.doi.org/10.1080/0143116031000115328.
Watson, K., 1975. Geologic applications of thermal infrared images. Proc. IEEE 63 (1), 128–137. http://dx.doi.org/10.1109/PROC.1975.9712.
Watson, K., 2000. A diurnal animation of thermal images from a day-night pair. Remote Sens. Environ. 72 (2), 237–243. http://dx.doi.org/10.1016/S0034-4257(99)00106-6.
Weng, Q., 2009. Thermal infrared remote sensing for urban climate and environmental studies: methods, applications, and trends. ISPRS J. Photogramm. Remote Sens. 64 (4), 335–344. http://dx.doi.org/10.1016/j.isprsjprs.2009.03.007.
Weng, Q., Fu, P., 2014. Modeling diurnal land temperature cycles over Los Angeles using downscaled GOES imagery. ISPRS J. Photogramm. Remote Sens. 97, 78–88. http://dx.doi.org/10.1016/j.isprsjprs.2014.08.009.
Xue, Y., Cracknell, A.P., 1995. Advanced thermal inertia modelling. Int. J. Remote Sens. 16 (3), 431–446. http://dx.doi.org/10.1080/01431169508954411.
Zakšek, K., Oštir, K., 2012. Downscaling land surface temperature for urban heat island diurnal cycle analysis. Remote Sens. Environ. 117, 114–124. http://dx.doi.org/10.1016/j.rse.2011.05.027.
Zakšek, K., Schroedter-Homscheidt, M., 2009. Parameterization of air temperature in high temporal and spatial resolution from a combination of the SEVIRI and MODIS instruments. ISPRS J. Photogramm. Remote Sens. 64 (4), 414–421. http://dx.doi.org/10.1016/j.isprsjprs.2009.02.006.
Zhan, W., Huang, F., Quan, J., Zhu, X., Gao, L., Zhou, J., Ju, W., 2016. Disaggregation of remotely sensed land surface temperature: a new dynamic methodology. J. Geophys. Res. Atmos. 121 (18), 10538–10554. http://dx.doi.org/10.1002/2016JD024891.
Zhan, W., Zhou, J., Ju, W., Li, M., Sandholt, I., Voogt, J., Yu, C., 2014. Remotely sensed soil temperatures beneath snow-free skin-surface using thermal observations from tandem polar-orbiting satellites: an analytical three-time-scale model. Remote Sens. Environ. 143 (6), 1–14. http://dx.doi.org/10.1016/j.rse.2013.12.004.
Zhou, J., Chen, Y., Zhang, X., Zhan, W., 2013. Modelling the diurnal variations of urban heat islands with multi-source satellite data. Int. J. Remote Sens. 34 (21), 7568–7588. http://dx.doi.org/10.1080/01431161.2013.821576.
Zhu, L., Zhou, J., Liu, S., Li, G., 2017. Temporal normalization research of airborne land surface temperature. J. Remote Sens. 21 (2), 193–205. http://dx.doi.org/10.11834/jrs.20176103.
Zhang, X., Pang, J., Li, L., 2015. Estimation of land surface temperature under cloudy skies using combined diurnal solar radiation and surface temperature evolution. Remote Sens. 7 (1), 905–921. http://dx.doi.org/10.3390/rs70100905.